UCLA
UCLA Previously Published Works

Title

18F-labeled anti-human CD20 cys-diabody for same-day immunoPET in a model of aggressive B cell lymphoma in human CD20 transgenic mice

Permalink

https://escholarship.org/uc/item/0gt2g894

Journal

European Journal of Nuclear Medicine and Molecular Imaging, 46(2)

ISSN

1619-7070

Authors

Zettlitz, Kirstin A
Tavaré, Richard
Tsai, Wen-Ting K
et al.

Publication Date

2019-02-01

DOI

10.1007/s00259-018-4214-x

Peer reviewed

ORIGINAL ARTICLE

^{18}F-labeled anti-human CD20 cys-diabody for same-day immunoPET in a model of aggressive B cell lymphoma in human CD20 transgenic mice

Kirstin A. Zettlitz[1,2] · Richard Tavaré[1,3] · Wen-Ting K. Tsai[1] · Reiko E. Yamada[4] · Noel S. Ha[1,5] · Jeffrey Collins[1] · R. Michael van Dam[1,5] · John M. Timmerman[4] · Anna M. Wu[1,2]

Abstract

Purpose Metabolic imaging using [^{18}F]FDG is the current standard for clinical PET; however, some malignancies (e.g., indolent lymphomas) show low avidity for FDG. The majority of B cell lymphomas express CD20, making it a valuable target both for antibody-based therapy and imaging. We previously developed PET tracers based on the humanised anti-CD20 antibody obinutuzumab (GA101). Preclinical studies showed that the smallest bivalent fragment, the cys-diabody (GAcDb, 54.5 kDa) with a peak uptake at 1–2 h post-injection and a biological half-life of 2–5 h, is compatible with short-lived positron emitters such as fluorine-18 (^{18}F, $t_{1/2}$ 110 min), enabling same-day imaging.

Methods GAcDb was radiolabeled using amine-reactive *N*-succinimidyl 4-[^{18}F]-fluorobenzoate ([^{18}F]SFB), or thiol-reactive *N*-[2-(4-[^{18}F]-fluorobenzamido)ethyl]maleimide ([^{18}F]FBEM) for site-specific conjugation to C-terminal cysteine residues. Both tracers were used for immunoPET imaging of the B cell compartment in human CD20 transgenic mice (hCD20TM). [^{18}F]FB-GAcDb immunoPET was further evaluated in a disseminated lymphoma (A20-hCD20) syngeneic for hCD20TM and compared to [^{18}F]FDG PET. Tracer uptake was confirmed by ex vivo biodistribution.

Results The GAcDb was successfully ^{18}F-radiolabeled using two different conjugation methods resulting in similar specific activities and without impairing immunoreactivity. Both tracers ([^{18}F]FB-GAcDb and [^{18}F]FBEM-GAcDb) specifically target human CD20-expressing B cells in transgenic mice. Fast blood clearance results in high contrast PET images as early as 1 h post injection enabling same-day imaging. [^{18}F]FB-GAcDb immunoPET detects disseminated lymphoma disease in the context of normal tissue expression of hCD20, with comparable sensitivity as [^{18}F]FDG PET but with added specificity for the therapeutic target.

Conclusions [^{18}F]FB-GAcDb and [^{18}F]FBEM-GAcDb could monitor normal B cells and B cell malignancies non-invasively and quantitatively in vivo. In contrast to [^{18}F]FDG PET, immunoPET provides not only information about the extent of disease but also about presence and localisation of the therapeutic target.

Keywords Anti-CD20 cys-diabody · Antibody fragments · ImmunoPET · ^{18}F · B cell lymphoma · Same-day imaging

---

✉ Kirstin A. Zettlitz
kzettlitz@coh.org

Anna M. Wu
awu@coh.org

[1] Crump Institute for Molecular Imaging, Department of Molecular and Medical Pharmacology, David Geffen School of Medicine, University of California, Los Angeles, Los Angeles, CA 90095, USA

[2] Present address: Department of Molecular Imaging and Therapy, Beckman Research Institute, City of Hope, 1500 E Duarte Rd, Duarte, CA 91010, USA

[3] Present address: Regeneron Pharmaceuticals, Inc, 777 Old Saw Mill River Road, Tarrytown, NY 10591, USA

[4] Division of Hematology & Oncology, Department of Medicine, University of California, Los Angeles, Los Angeles, CA 90095, USA

[5] Department of Bioengineering, Samueli School of Engineering, University of California, Los Angeles, Los Angeles, CA 90095, USA

Introduction

Positron emission tomography (PET) using [^{18}F]fluoro-deoxyglucose (FDG) combined with computed tomography (CT) has become the standard clinical imaging application in lymphoma [1]. FDG PET/CT plays a crucial role in staging [2–4] and response evaluation in Hodgkin (HL) and non-Hodgkin lymphomas (NHL) [5, 6]. While metabolic imaging facilitates noninvasive imaging of lymphoma, the only conclusive diagnostic method for HL and NHL is highly invasive tissue biopsies that delineate the genetic and phenotypic differences between lymphoma types [7].

Further limitations of FDG include nonspecific uptake in nonmalignant tissues (e.g., inflamed tissues) and in different cell types of the tumour microenvironment with high metabolic activity (e.g., immune cells, stromal cells) [8]. Malignant lymphomas often exist as disseminated disease with single or confluent tumours presenting a wide range of volumes and heterogenous uptake [3, 9]. Some forms of NHL show low FDG avidity, e.g., MALT marginal zone lymphoma, small lymphocytic lymphoma and cutaneous B cell lymphoma [2, 7].

ImmunoPET, utilising the specificity of antibodies, could provide additional phenotypic information regarding the presence or modulation of a B cell specific target, and has the potential to improve diagnosis, therapy selection and patient stratification. The B cell antigen CD20 is expressed on B lymphocytes, with minimal or no expression on early pre-B cells, plasma cells or other normal cells. CD20 expression on B cell malignancies is an important biomarker and therapy target, as evidenced by the clinical success of anti-CD20 monoclonal antibodies (mAbs) rituximab, ofatumumab, obinutuzumab and the radioimmunotherapeutic ibritumomab tiuxetan [10, 11]. Anti-CD20 mAbs have also shown clinical benefits in the treatment of the autoimmune disorder rheumatoid arthritis (RA) and are in clinical trials for systemic lupus erythematosus (SLE) and multiple sclerosis (MS) [12].

While radiolabeled full-length IgGs have been successfully used for PET imaging [13, 14], their long plasma half-life and their therapeutic activity are disadvantageous for both prompt and repeated imaging. We previously developed CD20-specific immunoPET tracers using obinutuzumab (GA101) based antibody fragments radiolabeled with zirconium-89 (^{89}Zr) or iodine-124 (^{124}I) and showed antigen specific targeting of malignant and endogenous B cells in vivo [15]. The smallest bivalent fragment, the cys-diabody (GAcDb, 55 kDa), presents a suitable compromise between tumour uptake (peak uptake 1-2 h) and blood clearance ($t_{1/2}$ 2-5 h) that aligns with the half-life of ^{18}F ($t_{1/2}$ 110 min), the most broadly used PET radionuclide [16]. ^{18}F-radiolabeling of GAcDb could enable same-day imaging and lower radiation

exposure compared with the longer-lived ^{124}I ($t_{1/2}$ 4.2 days) and ^{89}Zr ($t_{1/2}$ 3.3 days). Furthermore, ^{18}F has almost ideal imaging properties, with a high positron yield (97%), low mean positron range (0.5 mm) and no simultaneous gamma ray emission that would increase background.

Although ^{18}F is readily available in most radiopharmacies, the synthesis of prosthetic groups and the generation of ^{18}F-labeled antibody fragments can require elaborate procedures under time constraints caused by the short half-life. These challenges can be overcome by automated chemistry stations that enable the synthesis of prosthetic groups for radiofluorination of peptides and proteins [17, 18]. The most common prosthetic group, N-succinimidyl 4-[^{18}F]-fluorobenzoate ([^{18}F]SFB), forms a stable amide bond by reacting with primary amine groups (lysine residues) [19]. [^{18}F]SFB has been used successfully for the radiolabeling of diabodies [20, 21], scFv [22] and nanobodies [23, 24]. Alternatively, the thiol-reactive labelling agent N-[2-(4-[^{18}F]-fluorobenzamido)ethyl]maleimide ([^{18}F]FBEM) can be used for site-specific conjugation to cysteine residues [25], as shown for affibodies [26], and epidermal growth factor (EGF) [27].

For preclinical imaging evaluation of the ^{18}F-labeled anti-human CD20 GAcDb, a major consideration is the selection of a murine model of lymphoma. Most common are human xenograft models, based on homogenous cell lines, and implanted subcutaneously into immunodeficient mice. However, these xenograft models do not represent lymphomas that directly arise from immune cells, and they lack the complex interactions between cancer and the immune system that are of great interest in therapeutic and imaging studies. Transgenic models of lymphoma (e.g., altered c-Myc and Bcl-2 proteins) represent more realistic disease models [28, 29], but are not useful for studying antibodies targeting human antigens.

In this study, we used a transgenic mouse model expressing human CD20 (hCD20TM, BALB/c x hCD20) specifically on mature B cells (splenic B cells, B cells of lymph node, peritoneal cavity and peripheral blood) to compare in vivo targeting and biodistribution of GAcDb labeled with either [^{18}F]SFB or site-specifically with [^{18}F]FBEM [30]. For a more physiologically and clinically relevant lymphoma model we used a syngeneic B cell lymphoma cell line transduced to express human CD20 (A20-hCD20) [31]. When injected intravenously into hCD20TM, the disseminated lymphoma grows nodular lesions primarily in the liver and spleen, mimicking the natural development of an aggressive human lymphoma (diffuse large B cell lymphoma, DLBCL) [32]. This lymphoma model enables imaging in the context of normal tissue expression of hCD20. Serial imaging using [^{18}F]FDG PET/CT followed the next day by [^{18}F]FB-GAcDb immunoPET/CT was conducted on mice with limited or extensive disease and on mice injected with antigen negative A20 cells as control.

Materials and methods

Radiosynthesis

2-deoxy-2-[^{18}F]fluoro-D-glucose ([^{18}F]FDG), N-succinimidyl 4-[^{18}F]-fluorobenzoate ([^{18}F]SFB) and N-[2-(4-[^{18}F]fluorobenzamido)ethyl]maleimide ([^{18}F]FBEM) [25] were generated using the ELIXYS automated radiosynthesizer (Sofie Biosciences) [33]. Radiochemical purity was confirmed to be >95% by radio-HPLC, and radiochemical identity was confirmed in analytical HPLC by comparison with co-injected standard.

Radiolabeling of GAcDb

Cloning, production and purification of the obinutuzumab-based cys-diabody GAcDb has been described previously [15].

For random labelling to lysine residues, [^{18}F]SFB was resuspended in sodium borate buffer (150-300 MBq in 100 μL SBB 50 μmol/L, pH 8.7) and incubated with GAcDb (100-200 μg in 200 μL SBB) for 10 min at 34 °C. For site-specific radiolabeling [^{18}F]FBEM (330 MBq in 30 μL PBS) was incubated with reduced (10-fold molar excess, 2 h, 22 °C, TCEP, Sigma-Aldrich) GAcDb (100 μg in 30 μL PBS) for 15 min at 22 °C. Excess prosthetic groups were separated from the conjugate using Micro Bio-Spin size exclusion columns (Bio-Rad) pre-blocked with PBS, 1%FBS. Labelling efficiency and radiochemical purity were analysed using ITLC strips (for monoclonal antibody preparation, Biodex Medical Systems) with saline as solvent (Wizard 3′ 1480 Automatic Gamma Counter, Perkin Elmer). The immunoreactive fraction of radiolabeled GAcDb was determined by incubation with excess antigen expressing cells (A20-hCD20) and control cells (A20) for 1 h at 22 °C as described previously [15].

Syngeneic disseminated B cell lymphoma model

All procedures performed in studies involving animals were in accordance with the ethical standards of the University of California Los Angeles (UCLA) Animal Research Committee. Murine A20 BALB/c B cell lymphoma line (ATCC) and A20 cells transduced with a lentivirus encoding the human CD20 gene (A20-hCD20, clone R2D2) [34] were cultured in RPMI1640 supplemented with 10% FBS and 50 μmol/L 2-mercaptoethanol (Life Technologies). Human CD20 transgenic mice (hCD20TM), a kind gift from Mark Shlomchik, Yale University, have been described previously [30, 34] and were backcrossed onto BALB/c backgrounds and genotypes confirmed by PCR (Fig. S1). A20 or A20-hCD20 cells were washed three times using Hank's Balanced Salt Solution (HBSS) buffer and injected intravenously (lateral tail vein, 1×10^6 cells/100 μL HBSS).

ImmunoPET/CT imaging, ROI analysis and biodistribution

PET imaging (Inveon, Siemens) was performed under 2% isoflurane anaesthesia followed by a CT scan (MicroCAT, Siemens). Optional FDG-PET (10 min static scan) was conducted 24 h prior to immunoPET imaging, using 3.7 MBq of [^{18}F]FDG, followed by 1 h conscious uptake. For immunoPET, mice were injected with 15–20 μg (3.7-7.4 MBq) of either [^{18}F]FB-GAcDb or [^{18}F]FBEM-GAcDb. One- or two-hour dynamic PET acquisitions were followed by ten minute static scans at 2, 4 and 6 h post injection (p.i.). PET images were reconstructed using maximum a posteriori (OSEM MAP) algorithm, and PET and CT images are presented as maximum intensity projection (MIP) overlays. AMIDE software was used for image analysis [35]. For quantitation of the PET signal in specific organs, 3D regions of interest (ROI) were drawn and the mean voxel value was converted to %ID/cc$_{ROI}$ using the decay corrected injected dose and an empirically determined cylinder factor for ^{18}F.

Ex vivo biodistributions were performed by weighing and gamma counting tissues and calculating %ID/g values based on standards containing 1% of the injected dose.

Statistical analysis

Data values are reported as mean ± SD unless indicated otherwise. Ex vivo biodistribution values are depicted as box-and-whiskers (min to max) graphs. For statistical analysis multiple t-tests (Holm-Sidak method, GraphPad Prism) were performed.

Results

Radiolabeling of GA101 cys-diabody (GAcDb)

GAcDb was successfully ^{18}F-radiolabeled using two different approaches. For random labelling, the amine reactive prosthetic group N-succinimidyl-4-[^{18}F]fluorobenzoate ([^{18}F]SFB) forms covalent amine bonds with surface exposed lysine residues ([^{18}F]FB-GAcDb, Fig. 1a). For site-specific conjugation to the C-terminal cysteine residues (cys-tag), the sulfhydryl reactive prosthetic group N-[2-(4-[^{18}F]fluorobenzamido)ethyl]maleimide ([^{18}F]FBEM) was used, resulting in [^{18}F]FBEM-GAcDb (Fig. 1b). SDS-PAGE analysis shows the unconjugated GAcDb migrating with an apparent molecular weight of approximately 55 kDa corresponding to the covalent homodimer (Fig. 1c, lane 1). Incubation with TCEP results in complete reduction of solely the solvent exposed C-terminal disulphide bond and the

Fig. 1 Radiolabeling of GA101 cys-diabody (GAcDb). a Schematic of random labelling using the amine reactive prosthetic group *N*-succinimidyl-4-[^{18}F]fluorobenzoate ([^{18}F]SFB) to deprotonated lysine residues (50 mM NaBO$_3$ pH 8.7) resulting in [^{18}F]FB-GAcDb. **b** Schematic of site-specific conjugation using the sulfhydryl reactive prosthetic group [^{18}F]-4-fluorobenzoamido-N-ethylamino-maleimide ([^{18}F]FBEM) to the C-terminal cysteine residues (after mild reduction using TCEP) resulting in [^{18}F]FBEM-GAcDb. **c** SDS-PAGE analysis of site-specific conjugation (non-reducing conditions). GAcDb (lane 1), with TCEP (lane 2), reoxidised after TCEP removal (lane 3), conjugated with [^{18}F]FBEM in the presence of TCEP (lane 4) or after TCEP removal (lane 5). **d** Size exclusion chromatography of FBEM-GAcDb and unconjugated GAcDb demonstrates that FBEM conjugation did not disrupt diabody conformation. Protein standards are indicated by *dashed lines*
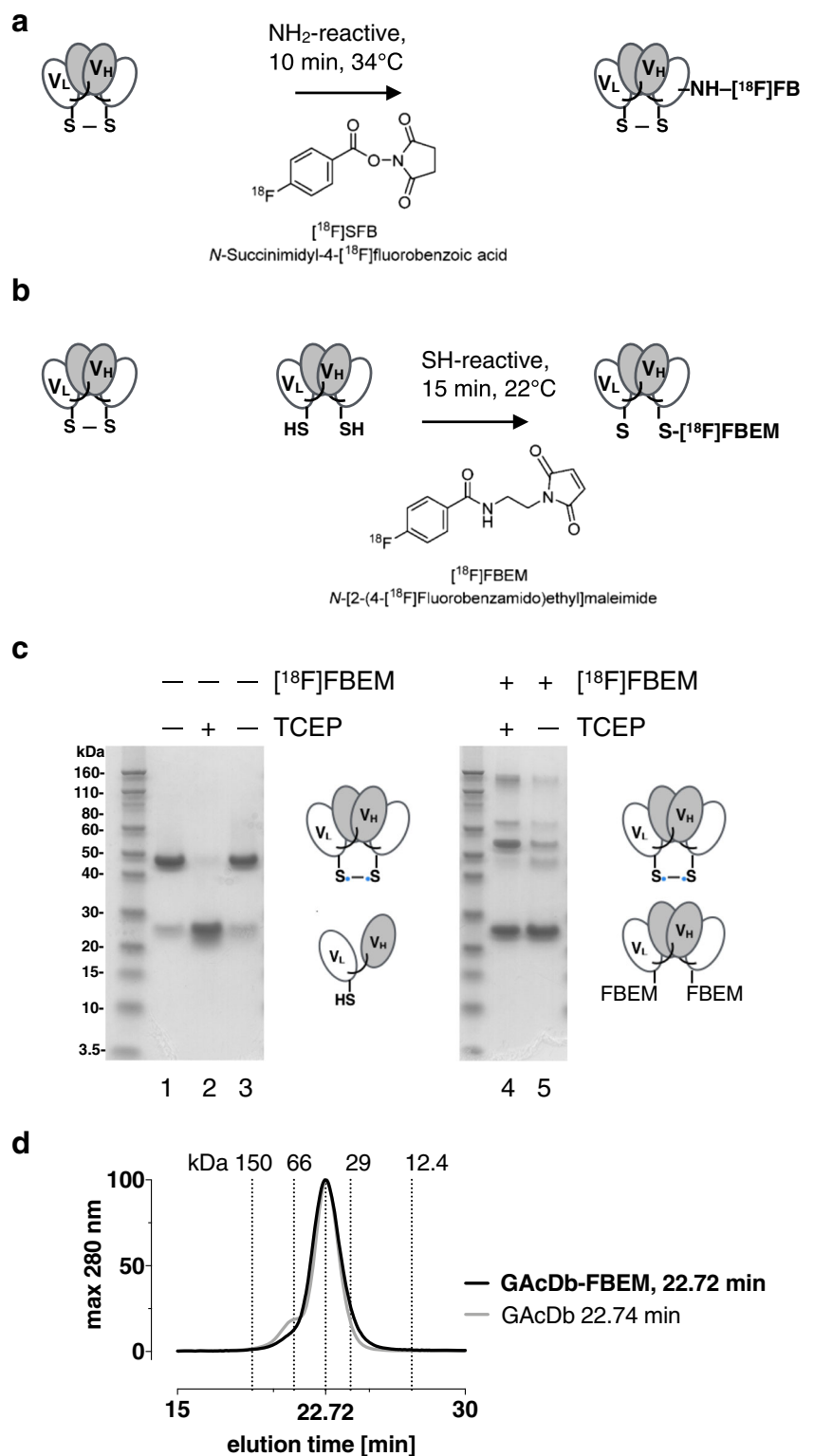
diabody migrates as scFv monomer (M$_W$ 27.3 kDa) (Fig. 1c, lane 2). After TCEP removal (by size exclusion spin column) the GAcDb reoxidises to its covalent dimeric conformation within 24 h (Fig. 1c, lane 3). Incubation of the reduced GAcDb with [^{18}F]FBEM and with TCEP present or with TCEP removed, leads to site-specific conjugation, blocks reoxidation of the cys-

tag and [^{18}F]FBEM-GAcDb migrates as monomer (Fig. 1c, lane 4, 5). Additional bands in lanes 4 and 5 are due to FBS blocking of the size exclusion spin columns used for purification of the conjugates. To confirm the stable non-covalent diabody conformation of FBEM-GAcDb, size exclusion chromatography was performed and the elution profile compared to unconjugated

GAcDb (Fig. 1d). Both proteins eluted as single peaks at 22.7 min, corresponding to the molecular weight of approximately 55 kDa, confirming that the FBEM conjugation did not disrupt the diabody conformation.

Both radiolabeling methods were carried out in about 30 min and resulted in comparable specific activities of 0.48 ± 0.19 MBq/μg for [18F]FB-GAcDb and 0.48 ± 0.11 MBq/μg for [18F]FBEM-GAcDb, respectively. Radiochemical purity after size exclusion spin column was >95% and 18F-radiolabeled GAcDb retained specific binding to CD20-expressing cells. Radiolabeling results are summarised in Table 1.

18F-labeled GAcDb targets B cells in human CD20 transgenic mice

[18F]FB-GAcDb or [18F]FBEM-GAcDb (15 μg) were injected i.v. into hCD20TM, and dynamic PET scans (1–2 h) followed by 10-min static scans of the same mouse at 2 and 4 h post injection (p.i.) were acquired (Fig. 2). [18F]FB-GAcDb (Fig. 2b) showed rapid targeting to the B cell containing spleen with activity visible as early as 10 min p.i. and peaking around 30–60 min p.i. The signal in the kidneys and the bladder increased over time indicating clearance/excretion of the tracer primarily through the kidneys and into the urine. Activity in the kidneys was highest around 1 h p.i. and decreased continuously while antigen-specific retention in the spleen was more steady, resulting in high-contrast PET images at 4 h p.i.

In comparison, [18F]FBEM-GAcDb (Fig. 2c) showed earlier (5 min p.i.) and higher target specific accumulation in the spleen peaking at 30 min p.i. followed by a steady decrease of the radioactivity signal. The signal in the heart (estimating the activity in the blood pool) decreased visibly from 10 min p.i. on, indicating a more rapid blood clearance compared with [18F]FB-GAcDb. Similar to [18F]FB-GAcDb, the site-specific conjugated [18F]FBEM-GAcDb showed primarily renal clearance with activity visible in the kidneys after 10 min and in the bladder at 30 min p.i. Approximately 60 min p.i. activity started to become visible in the gastrointestinal (GI) tract, and 2 h p.i. accumulation of radiometabolites in the gall

bladder (GB) suggest a secondary hepatobiliary clearance route.

HCD20TM imaged using the metabolic tracer [18F]FDG showed only non-specific background activity in the Harderian glands, heart, kidneys, intestines and bladder (Fig. 3a). In contrast, both anti-CD20 immunoPET tracers successfully visualised the normal tissue distribution of hCD20 in spleen and lymph nodes (rescaled images in Fig. 3b and c). Notably, the smallest (popliteal) lymph nodes visible in the immunoPET scans are only about 1 mm³ in size. Although the signal in the spleen at 4 h p.i. is comparable between the two tracers, the remaining activity in the intestines for [18F]FBEM-GAcDb obstructs the view of the abdominal area. In conclusion, both [18F]FB-GAcDb and [18F]FBEM-GAcDb show specific targeting of hCD20 B cells and optimised pharmacokinetics to enable same-day imaging.

18F-radiolabeling chemistry affects tracer biodistribution and excretion

Quantitative region of interest (ROI) analysis of the immunoPET scans was conducted for both tracers (Fig. 4a and c). For the randomly labeled [18F]FB-GAcDb, peak uptake in the target organ (spleen, ~18%ID/g$_{ROI}$) was reached between 1 and 2 h p.i. followed by slow decrease of activity thereafter. Activity in organs of clearance (kidneys) was highest around 1 h p.i. at 20%ID/g$_{ROI}$. Highest target-to-background ratio is achieved at later time points (> 2 h p.i.) when activity has sufficiently cleared from the blood (heart) and the kidneys (5–10%ID/g$_{ROI}$). The tracer half-life as calculated from the blood curve is t$_{1/2(\beta)}$ 68.8 min.

In contrast, the site-specifically labeled [18F]FBEM-GAcDb reached higher uptake in the spleen (38%ID/g$_{ROI}$) at earlier time points. Activity in organs of clearance (kidneys) peaked around 0.5 h p.i. at 15%ID/g$_{ROI}$. Therefore, to achieve high contrast images without obstruction by nonspecific activity in the GI tract, [18F]FBEM-GAcDb immunoPET would be most suitable when very early imaging time points are desired (around 1 h p.i.). The tracer half-life as calculated from the blood curve is t$_{1/2(\beta)}$ 78.3 min.

Ex vivo biodistribution of mice injected with either [18F]FB-GAcDb (4 h p.i., $n = 10$) or [18F]FBEM-GAcDb

Table 1 Radiolabeling of GA101 cys-diabody (GAcDb)

| Parameter	[18F]FB-GAcDb			[18F]FBEM-GAcDb		
	Mean	Standard deviation (SD)	Number (n)	Mean	Standard deviation (SD)	Number (n)
Labeling efficiency [%]	37.7	3.4	7	17.7	4.6	5
Specific activity [μCi/μg]	12.8	4.6	7	12.9	3.1	3
Radiochemical purity [%]	96.2	3.1	6	96.8	5.3	4
Immunoreactivity [%]	61.2	4.7	5	73.2	n.d.	1

Fig. 2 ImmunoPET imaging of hCD20 transgenic mice shows antigen specific retention in the spleen. a [^{18}F]FB-GAcDb immunoPET in wild type BALB/c mice, 5.6 MBq/15 μg, 10 min static scan at 1, 2 and 4 h p.i. **b** [^{18}F]FB-GAcDb immunoPET in hCD20TM, 14.8 MBq/24 μg, 5 min (5–30 min p.i.) and 10 min (1–2 h p.i.) frames from dynamic scan and 10 min static scan (4 h p.i.). **c** [^{18}F]FBEM-GAcDb immunoPET in hCD20TM, 4.3 MBq/12 μg. Primarily renal clearance (kidneys, *K*) and excretion into urine (bladder, *B*) is visible. Increased gallbladder (*GB*) and GI tract activity suggests secondary excretion of radiometabolites through the hepatobiliary system. ImmunoPET scans are depicted as whole body MIP PET/CT overlay
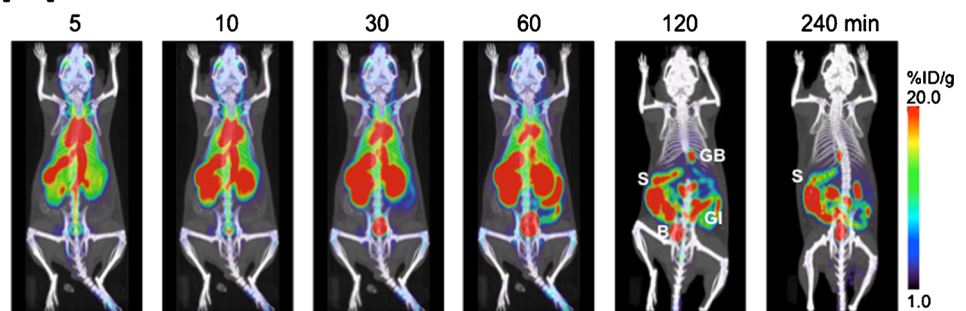

a [^{18}F]FB-GAcDb in BALB/c
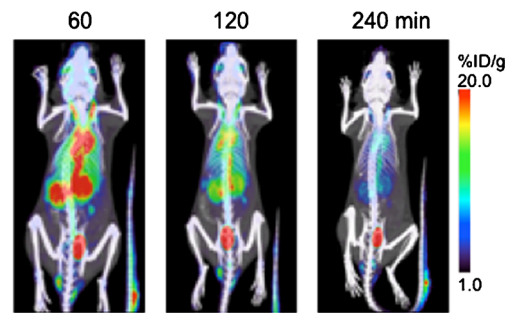
b [^{18}F]FB-GAcDb in hCD20TM
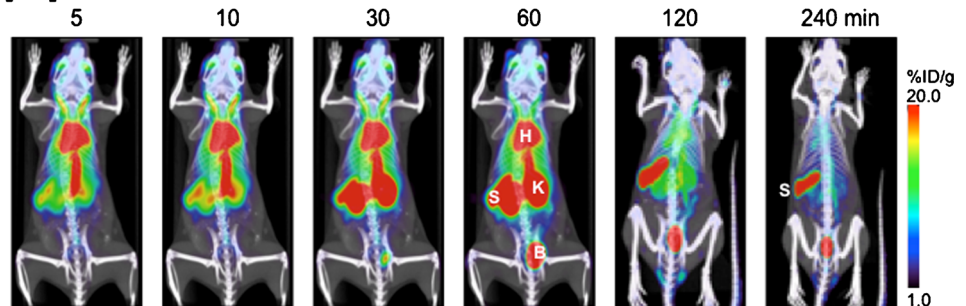
c [^{18}F]FBEM-GAcDb in hCD20TM

(6 h p.i., *n* = 4) confirmed the spleen as the organ with the highest uptake (Fig. 4b and d, Table S1). We did not observe a difference in %ID/g in the liver, although higher remaining activity in the intestines (GI tract including contents) at 6 h p.i. was confirmed for [^{18}F]FBEM-GAcDb indicating clearance through the hepatobiliary system and excretion with the feces.

[^{18}F]FB-GAcDb immunoPET of disseminated B cell lymphoma in the context of normal tissue expression of human CD20

Murine syngeneic B cell lymphoma cells (A20) engineered to express human CD20 (A20-hCD20) with an antibody binding capacity of ~45,000/cell (Fig. S2) were implanted into immunocompetent transgenic mice (BALB/c x hCD20). Intravenous injection of A20 lymphoma cells results in the dissemination of cells to the liver, and macroscopic examination showed prominent nodules on the liver surface after approximately 2–3 weeks (Fig. 5). Mice were grouped as 'limited disease' with multiple tumour lesions visible in the liver,

but without a change in average liver weight (1.55 ± 0.3 g, *n* = 4) and 'extensive disease' with significant tumour lesions visible and enlargement of livers (3.0 ± 0.7 g, *n* = 6). Target tissue uptake was compared to control groups of non-lymphoma bearing hCD20TM (*n* = 7) and hCD20TM injected with CD20-negative A20 (limited disease, liver weight: 1.32 ± 0.07 g, n = 4).

[^{18}F]FB-GAcDb was chosen to image disseminated B cell lymphoma despite its slower pharmacokinetics and lower spleen uptake because the primarily renal clearance results in low nonspecific background in the abdomen. The current standard for clinical PET [^{18}F]FDG was included for comparison. Mice were imaged with [^{18}F]FDG after 1 h conscious uptake and the following day the same mice were imaged with [^{18}F]FB-GAcDb (20 μg) at 4 h p.i.

In CD20-negative limited disease (A20) [^{18}F]FDG detects lymphoma lesions in the liver (Fig. 5a). [^{18}F]FB-GAcDb shows no nonspecific uptake in antigen negative metastases in the liver but targets CD20-expressing B-cells in the spleen and lymph nodes (Fig. 5a). CD20-positive (A20-hCD20)
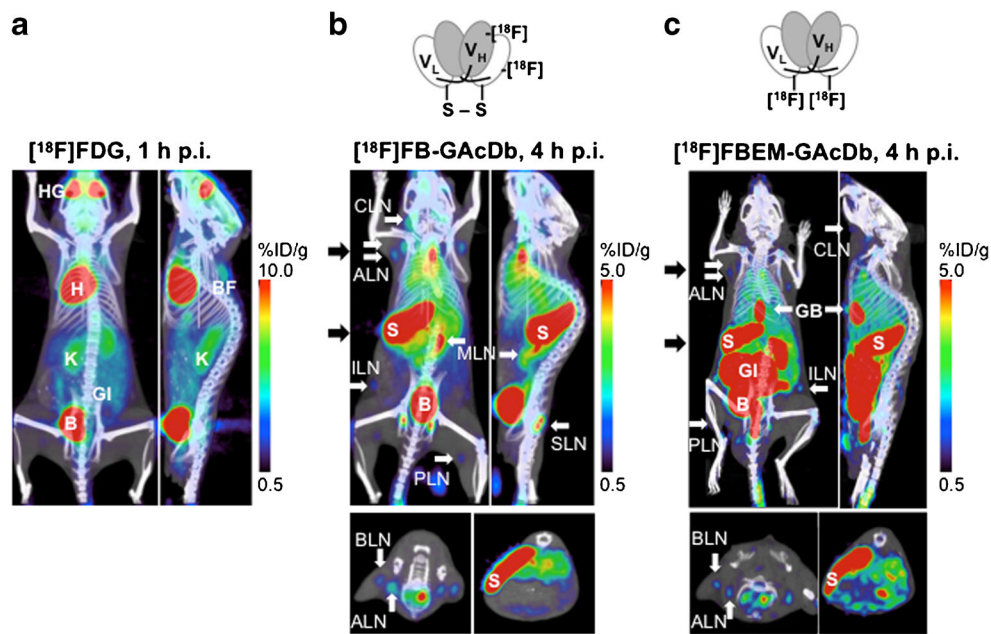
Fig. 3 Radiolabeling chemistry affects biodistribution/excretion of the tracer in hCD20 transgenic mice. a Mice (hCD20TM) were imaged after i.v. injection of approx. 3.7 MBq [^{18}F]FDG and conscious uptake for 1 h. Nonspecific uptake is visible in Harderian glands (HG), heart (H), brown fat (BF), kidneys (K), intestines (GI) and bladder (B). **b** The same mouse was imaged the following day by [^{18}F]FB-GAcDb immunoPET, 4 h p.i., and specific uptake in the spleen (S) and lymph nodes (*white arrows*) is visible: cervical (CLN), axillary (ALN) and brachial (BLN), inguinal (ILN), mesenteric (MLN), sciatic (SLN) and popliteal (PLN). **c** ImmunoPET imaging using [^{18}F]FBEM-GAcDb, 4 h p.i. Specific spleen and lymph node uptake is visible. The secondary secretion route of radiometabolites through the hepatobiliary system is indicated by the high signal in the gallbladder (GB) and the intestines (GI) and excretion of radioactivity with feces. Scans are depicted as PET/CT overlay, whole body MIP. *Black arrows* indicate the location of the 2 mm transverse section shown in the lower panel

limited disease in the liver was detected by [^{18}F]FDG-PET and by [^{18}F]FB-GAcDb with comparable sensitivity (Fig. 5b). [^{18}F]FDG also detected lymphoma nodules in the spleen. [^{18}F]FB-GAcDb specifically targeted CD20-positive lymphoid tissues and showed less nonspecific background. In mice with extensive disease, [^{18}F]FDG uptake is visible in the liver but is somewhat diffuse and obstructed by background activity in the heart and the kidneys (Fig. 5c). [^{18}F]FB-GAcDb immunoPET images of the same mice show distinct antigen-specific uptake in the liver nodules. CD20-positive lymphoid organs also show specific tracer uptake while less nonspecific background activity is seen in other tissues.

Ex vivo biodistribution confirmed the spleen as the organ with the highest uptake (17.7 ± 4.3%ID/g) in hCD20TM (Fig. 6, Table S2). Average uptake in the normal liver was 1.5 ± 0.5%ID/g. In CD20-positive lymphoma bearing mice (A20-hCD20), uptake in the liver was significantly higher for mice with both limited or extensive disease (2.4 ± 0.2%ID/g, $p = 0.0037$ and 4.8 ± 1.2%ID/g, $p < 0.0001$, respectively) and was not significantly different in mice with antigen-negative disease (A20, 1.1 ± 0.2%ID/g). This was further corroborated by the significantly increased total uptake in the liver of 3.7 ± 0.7%ID ($p = 0.0013$) for limited disease and 14.7 ± 5.6%ID ($p < 0.0001$) for extensive disease compared with 1.8 ± 0.7%ID in hCD20TM and 1.4 ± 0.3%ID in antigen negative disease.

At the same time, the uptake in the spleen decreased in mice with limited and extensive disease (10.7 ± 3.0 and 6.9 ± 2.0%ID/g, respectively) compared with hCD20TM, presumably due to the antigen sink effect caused by higher tumour burden. In contrast, the lower uptake value (9.6 ± 2.8%ID/g) in the spleen of mice injected with CD20-negative A20 lymphoma cells is likely caused by increased mass due to tumour growth in the spleen (hCD20TM: 0.11 ± 0.01 g; A20: 0.14 ± 0.05 g; A20-hCD20 lim: 0.15 ± 0.04 g; A20-hCD20 ext.: 0.22 ± 0.07 g).

Discussion

Metabolic imaging by [^{18}F]FDG PET has become the clinical standard in the assessment of patients with aggressive non-Hodgkin lymphoma (NHL) both for initial diagnosis and for response after therapy. The most prevalent subtypes of aggressive NHL (DLBCL, MCL, FL) are usually FDG-avid, and FDG PET/CT can lead to upstaging in 10–20% of cases compared with CT only [2], while low grade indolent lymphoma can show little to no uptake of FDG. A molecular imaging application that is specific for a tumour associated antigen could facilitate visualisation of FDG-inert lymphomas and/or complement FDG PET with phenotypic information.

Fig. 4 Ex vivo biodistribution of hCD20TM. **a** Quantitative ROI analysis of [18F]FB-GAcDb immunoPET. **b** Ex vivo biodistribution of [18F]FB-GAcDb 4 h p.i. confirms high uptake in the spleen and lymph nodes. Remaining activity in the kidneys suggests renal clearance. **c** Quantitative ROI analysis of [18F]FBEM-GAcDb immunoPET. **d** Ex vivo biodistribution of [18F]FBEM-GAcDb, 6 h p.i. confirms the spleen as the organ with the highest uptake
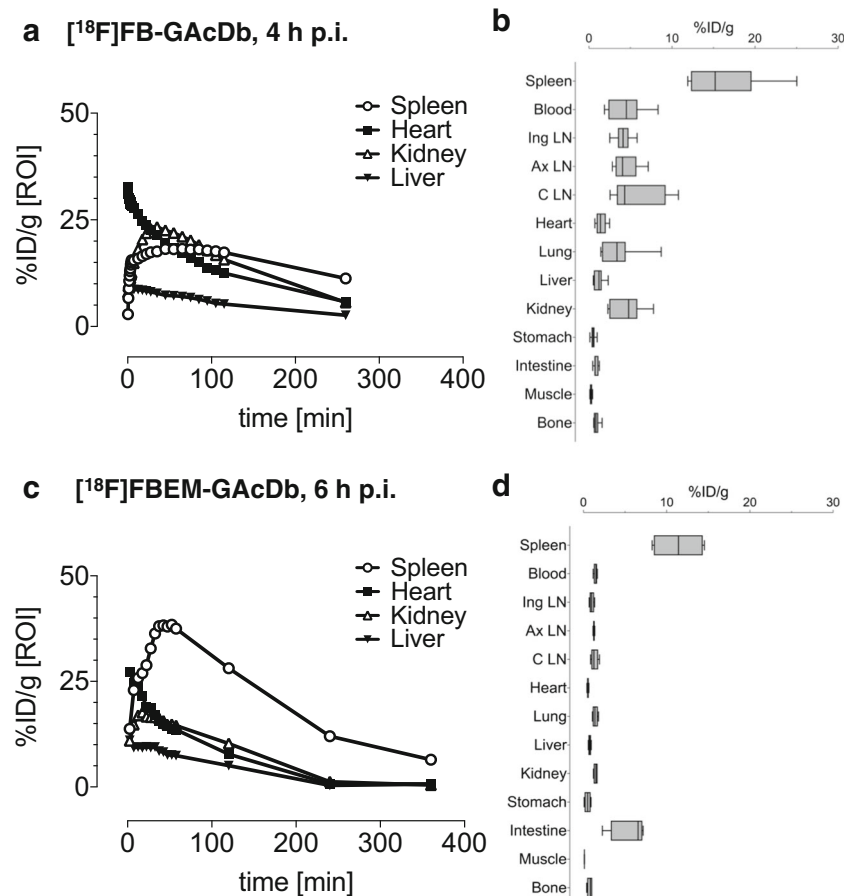
We previously developed a small bivalent antibody fragment (cys-diabody, GAcDb) based on the humanised, therapeutic, human CD20-specific antibody obinutuzumab (GA101), and confirmed specificity for B cells in vivo [15]. In this work, we successfully radiolabeled GAcDb using prosthetic groups [18F]SFB and [18F]FBEM [25, 36]. [18F]FB-GAcDb and [18F]FBEM-GAcDb immunoPET showed rapid (within 4–6 h p.i.) and antigen-specific targeting of CD20-expressing B cells in vivo. Furthermore, [18F]FB-GAcDb immunoPET/CT was successfully used to visualise a syngeneic disseminated lymphoma model for DLBCL (A20-hCD20) in the context of endogenous CD20 expression with comparable sensitivity as [18F]FDG PET/CT but added specificity for the therapeutic target.

A major motivation for combining 18F with the diabody format is the rapid clearance of the tracer, resulting in high contrast immunoPET images at early time points; thus, enabling same-day-imaging. At the same time, minimisation of radiation dose and exposure for the patient is a main feature of short-lived radionuclides, particularly with an almost pure positron emitter such as 18F.

The impact of the radiolabeling method on the biodistribution and pharmacokinetics of GAcDb was evaluated in a human CD20 transgenic mouse model (hCD20TM). Both labelling strategies were executed with similar reaction times and resulted in comparable specific activities; however, the random labelling to lysine residues using [18F]SFB bears the risk of labelling lysines located at or in the antigen binding sites. In contrast, the site-specific conjugation using [18F]FBEM is constrained to the C-terminus, away from the antigen binding site and thereby prevents interference with binding. The immune reactive fractions of [18F]FB-GAcDb and [18F]FBEM-GAcDb were comparable to each other (ranging from 61 to 73%) and to previously published data for 124I- and 89Zr-labeled GAcDb [15] confirming that the [18F]-radiolabeling did not impair binding to hCD20-expressing cells.

[18F]FB-GAcDb and [18F]FBEM-GAcDb differed in their blood clearance and biodistribution in hCD20TM. The site-specifically labeled [18F]FBEM-GAcDb showed earlier and higher spleen uptake and correlating faster serum clearance compared with [18F]FB-GAcDb. While smaller antibody fragments are filtered by the glomerulus, they are subsequently reabsorbed and catabolised to smaller peptides which is the major elimination process of antibody drugs. However, activity visible in the gallbladder and later in the gastrointestinal tract (GI) suggests unfavourable hepatobiliary excretion of [18F]FBEM-GAcDb radiometabolites, rendering it suitable only for imaging at early time points or outside the lower

Fig. 5 ImmunoPET of disseminated B cell lymphoma in the context of normal tissue expression of human CD20. Murine syngeneic lymphoma cells (A20 ± hCD20) were injected intravenously into immunocompetent hCD20 transgenic mice (BALB/c x hCD20) and result in the formation of liver metastases. **a** CD20-negative limited disease. **b** CD20-positive limited disease. **c** CD20-positive extensive disease. Mice were imaged with [18F]FDG (3.7 MBq, left panel) on day 14 (**a,b**) or day 20 (**c**). The same mice were imaged the following day with [18F]FB-GAcDb (6.7–11.2 MBq/15 μg, right panel). All images are displayed as whole body MIP PET/CT overlay of the coronal and sagittal view. The lower panel shows a 2-mm section of the liver as indicated by the *white arrow* (M = metastases; S = spleen)
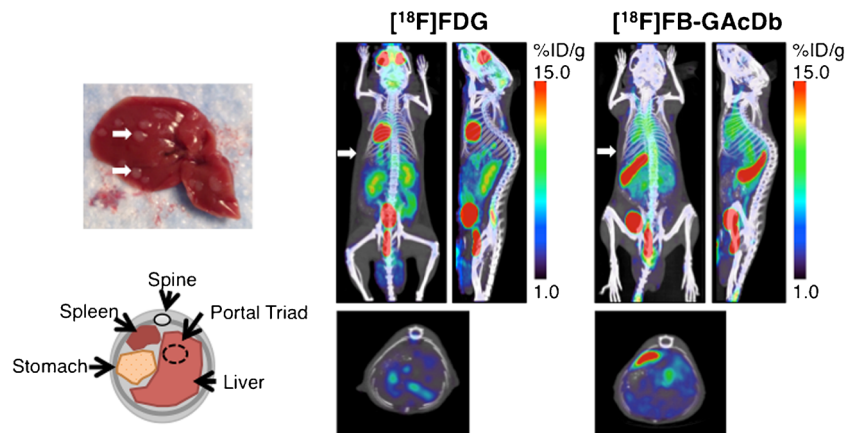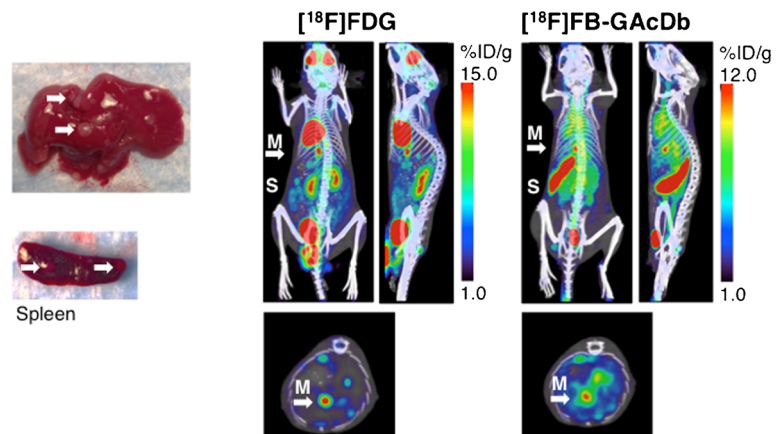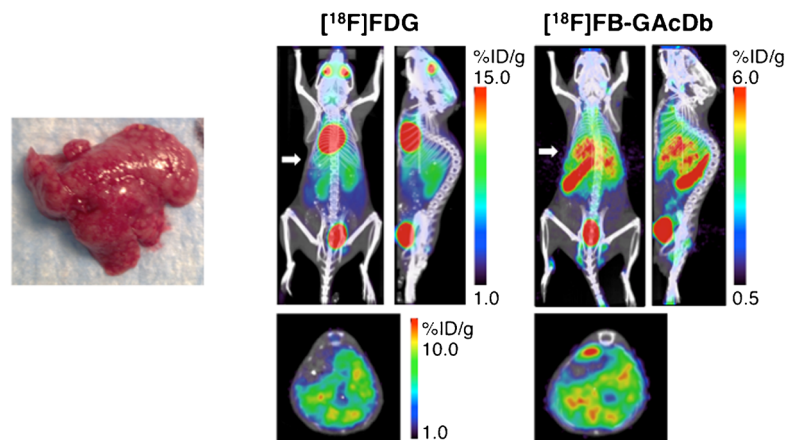

abdomen in mice. [18F]FB-GAcDb showed more favourable in vivo pharmacokinetics despite slower blood clearance and higher renal accumulation of activity, since excretion occurred exclusively through the kidneys and into the urine. These findings indicate that following glomerular filtration, reabsorption into renal cells and lysosomal degradation, metabolised peptides or mono-amino acid-adducts ([18F]FB-lysine and [18F]FBEM-cysteine, respectively) of different size

and charge are retained or transported back to the cell surface through different mechanisms [37, 38]. To prevent long residence times of radiometabolites and renal toxicity, tubular reabsorption can be blocked by infusion of basic amino acids (lysine, arginine) or polygelines (e.g., Gelofusine®) [39–41]. Importantly, no defluorination of 18F-labeled GAcDb was observed for either conjugation method, as there is no bone uptake visible in the PET scans at any time.

In this study, the smallest detectable structures (popliteal lymph nodes) in the hCD20TM were approximately ~1 mg in size, containing ~10^6 cells, with 30% B cells in the mouse lymph node [42]. While normal human B cells express around 100,000 CD20 molecules per cells, the transgenic mouse model is described as expressing about 7-fold lower CD20 levels per cell compared to B cells from human peripheral blood [30, 43]. This would suggest that [18F]FB-GAcDb immunoPET is able to detect an estimated 300,000 cells with an antigen density of ~15,000 CD20/cell in a mouse lymph node.

The syngeneic and immunocompetent lymphoma model (A20 in BALB/c mice) has been used extensively for preclinical evaluation of lymphoma therapies because it resembles the invasion course of aggressive human lymphoma (liver, spleen and mesenteric lymph nodes) [44–47]. Furthermore, a study by Chaise et al. evaluated [18F]FDG PET for early detection of therapy response in the A20 model, showing high level FDG uptake and the feasibility of non-invasive monitoring of A20 tumour growth, especially for intra-abdominal nodules that are poorly accessible to examination [32].

In the present study, we used A20 lymphoma cells transfected to express hCD20 in hCD20 transgenic BALB/c mice to show the practicability and relevance of lymphoma imaging in context of the endogenous B cell compartment. [18F]FB-GAcDb immunoPET detected small lymphoma nodules in the liver of hCD20TM with limited A20-hCD20 disease similar to [18F]FDG PET. Additionally, [18F]FB-GAcDb immunoPET provides phenotypic information (presence of

Fig. 6 Ex vivo biodistribution of [18F]FB-GAcDb, 4 h p.i. Ex vivo biodistributions were conducted after the last scan for each group: hCD20TM ($n = 7$), A20-hCD20 limited disease ($n = 4$), A20-hCD20 extensive disease ($n = 6$) and A20 limited disease ($n = 4$). %ID/g values were calculated based on 1% injected dose standards and are depicted as box-and-whisker plot (min-max)
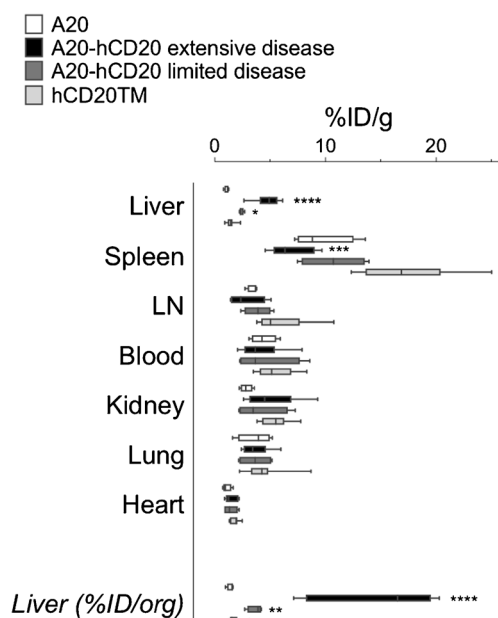
target) and assesses the whole body distribution of CD20-expressing B cells. Even though the detection of very small lesions is limited by scanner resolution (1.5–1.8 mm for Inveon PET) the increased liver uptake in the A20-hCD20 limited disease group was significantly different from healthy liver or antigen negative disease (A20), suggesting that [18F]FB-GAcDb immunoPET could detect tumour growth before lesions are large enough to be visible individually in the PET scan. Specificity of [18F]FB-GAcDb was confirmed in CD20-negative A20 lymphoma, that showed no tumour uptake.

The influence of tumour mass and antigen sink on the biodistribution and uptake values of the radiolabeled antibody fragment (protein dose 15 μg) was more pronounced in mice with extensive A20-hCD20 lymphoma, with liver uptake significantly higher and spleen uptake lower compared with healthy hCD20TM or limited disease. These results indicate that anti-CD20 immunoPET could be a valuable tool for determining dosimetry, e.g., for anti-CD20 radioimmunotherapy or other CD20 targeting therapies.

The ability to monitor disseminated disease in immunocompetent mice is crucial for evaluating lymphoma therapies because the tumour microenvironment in disseminated disease can differ from subcutaneous models of lymphoma and plays an important role in the immune response induced by therapy [48]. While [18F]FDG PET could predict therapy response by visualising altered cellular metabolism before measurable changes in tumour growth are induced [32], the CD20-specific [18F]FB-GAcDb immunoPET could distinguish cancer cells from other highly metabolically active cells present in the tumour microenvironment (pseudo-progression caused by infiltrating immune cells or inflammatory cells, e.g., activated macrophages or neutrophils).

Furthermore, anti-CD20 immunoPET could detect down regulation or loss of cell surface CD20, which might be one of several mechanisms of acquired resistance to rituximab. Several groups report a CD20-negative phenotypic switch after rituximab therapy [49]. Hiraga et al. showed that CD20 mRNA and protein expression can be restored and therefore seems regulated by epigenetic mechanisms [50]. Other groups have shown down-regulation of CD20 protein surface expression by FcRIIb-mediated internalisation or removal of antigen/antibody complexes by monocytes (trogocytosis) [51, 52].

In conclusion, we presented novel 18F-labeled anti-human CD20 antibody fragments for same-day immunoPET and showed their ability to detect both endogenous B cells and malignant B cells in vivo. Because GAcDb is based on the humanised, therapeutic antibody obinutuzumab it has potential for clinical translation for imaging in B cell lymphoma. [18F]FB-GAcDb immunoPET could complement [18F]FDG PET and improve diagnosis, staging, patient stratification, treatment strategy, and dosimetry. One possible clinical

application for anti-CD20 immunoPET could be prior to anti-CD20 radioimmunotherapy (RIT, ^{90}Y-ibritumomab tiuxetan, Zevalin®), where the antigen sink (tumour burden, spleen volume, amount of circulating B cells) greatly affects biodistribution and serum levels of the radioconjugate [14]. Monitoring response to therapy would be especially useful in B cell malignancies known to modulate CD20 cell surface expression.

Compliance with ethical standards

Conflict of interest JM Timmerman reports receiving commercial research grants from Bristol-Myers Squibb, Kite Pharma, and Valor Biotherapeutics, and is a consultant/ advisory board member for Celgene and Seattle Genetics. AM Wu holds ownership interest in and is a consultant/advisory board member for ImaginAb, Inc. No potential conflicts of interest were disclosed by the other authors.

Ethical approval All procedures performed in studies involving animals were in accordance with the ethical standards of the University of California Los Angeles (UCLA) Animal Research Committee. This article does not contain any studies with human participants performed by any of the authors.

References

1. Barrington SF, Johnson PWM. 18F-FDG PET/CT in lymphoma: has imaging-directed personalized medicine become a reality? J Nucl Med. 2017;58(10):1539–44.

2. Barrington SF, Mikhaeel NG, Kostakoglu L, Meignan M, Hutchings M, Mueller SP, et al. Role of imaging in the staging and response assessment of lymphoma: consensus of the International Conference on Malignant Lymphomas Imaging Working Group. J Clin Oncol. 2014;32(27):3048–58.

3. Meignan M, Itti E, Gallamini A, Younes A. FDG PET/CT imaging as a biomarker in lymphoma. Eur J Nucl Med Mol Imaging. 2015;42(4):623–33.

4. Adams HJ, Nievelstein RA, Kwee TC. Systematic Review on the Additional Value of 18F-Fluoro-2-Deoxy-D-Glucose Positron Emission Tomography in Staging Follicular Lymphoma. J Comput Assist Tomogr. 2017;41(1):98–103.

5. Kostakoglu L, Cheson BD. Current role of FDG PET/CT in lymphoma. Eur J Nucl Med Mol Imaging. 2014;41(5):1004–27.

6. Sun N, Zhao J, Qiao W, Wang T. Predictive value of interim PET/CT in DLBCL treated with R-CHOP: meta-analysis. Biomed Res Int. 2015;2015:648572.

7. England CG, Rui L, Cai W. Lymphoma: current status of clinical and preclinical imaging with radiolabeled antibodies. Eur J Nucl Med Mol Imaging. 2017;44(3):517–32.

8. Tang J, Salloum D, Carney B, Brand C, Kossatz S, Sadique A, et al. Targeted PET imaging strategy to differentiate malignant from inflamed lymph nodes in diffuse large B-cell lymphoma. Proc Natl Acad Sci USA. 2017;114(36):E7441–E9.

9. Friedberg JW, Chengazi V. PET scans in the staging of lymphoma: current status. Oncologist. 2003;8(5):438–47.

10. Goldsmith SJ. Radioimmunotherapy of lymphoma: Bexxar and Zevalin. Semin Nucl Med. 2010;40(2):122–35.

11. Lim SH, Beers SA, French RR, Johnson PW, Glennie MJ, Cragg MS. Anti-CD20 monoclonal antibodies: historical and future perspectives. Haematologica. 2010;95(1):135–43.

12. Du FH, Mills EA, Mao-Draayer Y. Next-generation anti-CD20 monoclonal antibodies in autoimmune disease treatment. Auto Immun Highlights. 2017;8(1):12.

13. Natarajan A, Habte F, Gambhir SS. Development of a novel long-lived immunoPET tracer for monitoring lymphoma therapy in a humanized transgenic mouse model. Bioconjug Chem. 2012;23(6):1221–9.

14. Muylle K, Flamen P, Vugts DJ, Guiot T, Ghanem G, Meuleman N, et al. Tumour targeting and radiation dose of radioimmunotherapy with (90)Y-rituximab in CD20+ B-cell lymphoma as predicted by (89)Zr-rituximab immuno-PET: impact of preloading with unlabelled rituximab. Eur J Nucl Med Mol Imaging. 2015;42(8):1304–14.

15. Zettlitz KA, Tavare R, Knowles SM, Steward KK, Timmerman JM, Wu AM. ImmunoPET of malignant and normal B cells with 89Zr- and 124I-labeled obinutuzumab antibody fragments reveals differential CD20 internalization in vivo. Clin Cancer Res. 2017;23(23):7242–7252.

16. Williams LE, Wu AM, Yazaki PJ, Liu A, Raubitschek AA, Shively JE, et al. Numerical selection of optimal tumor imaging agents with application to engineered antibodies. Cancer Biother Radiopharm. 2001;16(1):25–35.

17. Kiesewetter DO, Jacobson O, Lang L, Chen X. Automated radio-chemical synthesis of [18F]FBEM: a thiol reactive synthon for radiofluorination of peptides and proteins. Appl Radiat Isot. 2011;69(2):410–4.

18. Collins J, Waldmann CM, Drake C, Slavik R, Ha NS, Sergeev M, et al. Production of diverse PET probes with limited resources: 24 (18)F-labeled compounds prepared with a single radiosynthesizer. Proc Natl Acad Sci USA. 2017;114(43):11309–14.

19. Vaidyanathan G, Zalutsky MR. Labeling proteins with fluorine-18 using N-succinimidyl 4-[18F]fluorobenzoate. Int J Rad Appl Instrum B. 1992;19(3):275–81.

20. Cai W, Olafsen T, Zhang X, Cao Q, Gambhir SS, Williams LE, et al. PET imaging of colorectal cancer in xenograft-bearing mice by use of an 18F-labeled T84.66 anti-carcinoembryonic antigen diabody. J Nucl Med. 2007;48(2):304–10.

21. Liu K, Lepin EJ, Wang MW, Guo F, Lin WY, Chen YC, et al. Microfluidic-based 18F-labeling of biomolecules for immuno-positron emission tomography. Mol Imaging. 2011;10(3):168–76 **1-7**.

22. Sharma SK, Wuest M, Way JD, Bouvet VR, Wang M, Wuest FR. Synthesis and pre-clinical evaluation of an (18)F-labeled single-chain antibody fragment for PET imaging of epithelial ovarian cancer. Am J Nucl Med Mol Imaging. 2016;6(3):185–98.

23. Vaidyanathan G, Zalutsky MR. Synthesis of N-succinimidyl 4-[18F]fluorobenzoate, an agent for labeling proteins and peptides with 18F. Nat Protoc. 2006;1(4):1655–61.

24. Vaidyanathan G, McDougald D, Choi J, Koumarianou E, Weitzel D, Osada T, et al. Preclinical Evaluation of 18F-Labeled Anti-HER2 Nanobody Conjugates for Imaging HER2 Receptor Expression by Immuno-PET. J Nucl Med. 2016;57(6):967–73.

25. Cai W, Zhang X, Wu Y, Chen X. A thiol-reactive 18F-labeling agent, N-[2-(4-18F-fluorobenzamido)ethyl]maleimide, and

synthesis of RGD peptide-based tracer for PET imaging of alpha v beta 3 integrin expression. J Nucl Med. 2006;47(7):1172–80.

26. Kramer-Marek G, Kiesewetter DO, Martiniova L, Jagoda E, Lee SB, Capala J. [18F]FBEM-Z(HER2:342)-Affibody molecule-a new molecular tracer for in vivo monitoring of HER2 expression by positron emission tomography. Eur J Nucl Med Mol Imaging. 2008;35(5):1008–18.

27. Li W, Niu G, Lang L, Guo N, Ma Y, Kiesewetter DO, et al. PET imaging of EGF receptors using [18F]FBEM-EGF in a head and neck squamous cell carcinoma model. Eur J Nucl Med Mol Imaging. 2012;39(2):300–8.

28. Johnson NA, Savage KJ, Ludkovski O, Ben-Neriah S, Woods R, Steidl C, et al. Lymphomas with concurrent BCL2 and MYC translocations: the critical factors associated with survival. Blood. 2009;114(11):2273–9.

29. Li S, Lin P, Young KH, Kanagal-Shamanna R, Yin CC, Medeiros LJ. MYC/BCL2 double-hit high-grade B-cell lymphoma. Adv Anat Pathol. 2013;20(5):315–26.

30. Ahuja A, Shupe J, Dunn R, Kashgarian M, Kehry MR, Shlomchik MJ. Depletion of B cells in murine lupus: efficacy and resistance. J Immunol. 2007;179(5):3351–61.

31. Kim KJ, Kanellopoulos-Langevin C, Merwin RM, Sachs DH, Asofsky R. Establishment and characterization of BALB/c lymphoma lines with B cell properties. J Immunol. 1979;122(2):549–54.

32. Chaise C, Itti E, Petegnief Y, Wirquin E, Copie-Bergman C, Farcet JP, et al. [F-18]-Fluoro-2-deoxy-D: -glucose positron emission tomography as a tool for early detection of immunotherapy response in a murine B cell lymphoma model. Cancer Immunol Immunother. 2007;56(8):1163–71.

33. Lazari M, Lyashchenko SK, Burnazi EM, Lewis JS, van Dam RM, Murphy JM. Fully-automated synthesis of 16beta-(18)F-fluoro-5alpha-dihydrotestosterone (FDHT) on the ELIXYS radiosynthesizer. Appl Radiat Isot. 2015;103:9–14.

34. Bhatt S, Parvin S, Zhang Y, Cho HM, Kunkalla K, Vega F, et al. Anti-CD20-interleukin-21 fusokine targets malignant B cells via direct apoptosis and NK-cell-dependent cytotoxicity. Blood. 2017;129(16):2246–56.

35. Loening AM, Gambhir SS. AMIDE: a free software tool for multimodality medical image analysis. Mol Imaging. 2003;2(3):131–7.

36. Waldmann CM, Gomez A, Marchis P, Bailey ST, Momcilovic M, Jones AE, et al. An Automated Multidose Synthesis of the Potentiometric PET Probe 4-[(18)F]Fluorobenzyl-Triphenylphosphonium ([(18)F]FBnTP). Mol Imaging Biol. 2018;20(2):205–12.

37. Christensen EI, Nielsen S. Structural and functional features of protein handling in the kidney proximal tubule. Semin Nephrol. 1991;11(4):414–39.

38. Nielsen S. Endocytosis in proximal tubule cells involves a two-phase membrane-recycling pathway. Am J Phys. 1993;264(4 Pt 1):C823–35.

39. Vegt E, Wetzels JF, Russel FG, Masereeuw R, Boerman OC, van Eerd JE, et al. Renal uptake of radiolabeled octreotide in human subjects is efficiently inhibited by succinylated gelatin. J Nucl Med. 2006;47(3):432–6.

40. van Eerd JE, Vegt E, Wetzels JF, Russel FG, Masereeuw R, Corstens FH, et al. Gelatin-based plasma expander effectively reduces renal uptake of 111In-octreotide in mice and rats. J Nucl Med. 2006;47(3):528–33.

41. Akizawa H, Uehara T, Arano Y. Renal uptake and metabolism of radiopharmaceuticals derived from peptides and proteins. Adv Drug Deliv Rev. 2008;60(12):1319–28.

42. MartIn-Fontecha A, Sebastiani S, Hopken UE, Uguccioni M, Lipp M, Lanzavecchia A, et al. Regulation of dendritic cell migration to the draining lymph node: impact on T lymphocyte traffic and priming. J Exp Med. 2003;198(4):615–21.

43. Ginaldi L, De Martinis M, Matutes E, Farahat N, Morilla R, Catovsky D. Levels of expression of CD19 and CD20 in chronic B cell leukaemias. J Clin Pathol. 1998;51(5):364–9.

44. Briones J, Timmerman J, Levy R. In vivo antitumor effect of CD40L-transduced tumor cells as a vaccine for B-cell lymphoma. Cancer Res. 2002;62(11):3195–9.

45. Curti A, Parenza M, Colombo MP. Autologous and MHC class I-negative allogeneic tumor cells secreting IL-12 together cure disseminated A20 lymphoma. Blood. 2003;101(2):568–75.

46. Siegel S, Wagner A, Schmitz N, Zeis M. Induction of antitumour immunity using survivin peptide-pulsed dendritic cells in a murine lymphoma model. Br J Haematol. 2003;122(6):911–4.

47. Passineau MJ, Siegal GP, Everts M, Pereboev A, Jhala D, Wang M, et al. The natural history of a novel, systemic, disseminated model of syngeneic mouse B-cell lymphoma. Leuk Lymphoma. 2005;46(11):1627–38.

48. Pals ST, de Gorter DJ, Spaargaren M. Lymphoma dissemination: the other face of lymphocyte homing. Blood. 2007;110(9):3102–11.

49. Kennedy GA, Tey SK, Cobcroft R, Marlton P, Cull G, Grimmett K, et al. Incidence and nature of CD20-negative relapses following rituximab therapy in aggressive B-cell non-Hodgkin's lymphoma: a retrospective review. Br J Haematol. 2002;119(2):412–6.

50. Hiraga J, Tomita A, Sugimoto T, Shimada K, Ito M, Nakamura S, et al. Down-regulation of CD20 expression in B-cell lymphoma cells after treatment with rituximab-containing combination chemotherapies: its prevalence and clinical significance. Blood. 2009;113(20):4885–93.

51. Kennedy AD, Beum PV, Solga MD, DiLillo DJ, Lindorfer MA, Hess CE, et al. Rituximab Infusion Promotes Rapid Complement Depletion and Acute CD20 Loss in Chronic Lymphocytic Leukemia. J Immunol. 2004;172(5):3280–8.

52. Beers SA, French RR, Chan HT, Lim SH, Jarrett TC, Vidal RM, et al. Antigenic modulation limits the efficacy of anti-CD20 antibodies: implications for antibody selection. Blood. 2010;115(25):5191–201.